

Geometry of tilt (in)variance in scanned oblique plane microscopy

Manish Kumar¹ and Yevgenia Kozorovitskiy^{1,*}

¹Department of Neurobiology, Northwestern University

**Yevgenia.Kozorovitskiy@northwestern.edu*

Oblique plane microscopy (OPM) is a single objective light-sheet microscopy which performs three dimensional (3D) imaging by axial scan of the generated light-sheet. Recently, multiple techniques for lateral scan of the generated light-sheet in OPM have emerged. However, their suitability for geometrically distortion free 3D imaging, which essentially requires a constant tilt light-sheet scan, has not been evaluated. In this work, we use a geometrical optics approach and derive analytical relationship for the amount of tilt variance in planar mirror based scanned oblique plane illumination (SOPi) arrangement. We experimentally validate the derived relationship and use it to arrive at an optimized scanner geometry and to understand its associated limitations. We also discuss the effects of scanning on optical aberrations and 3D field of view in optimized, tilt invariant, lateral scanning OPM systems.

1 Introduction

Light-sheet microscopy is a powerful imaging technique based on optical sectioning. The conventional light-sheet microscopy configuration consists of two objectives orthogonally arranged around a sample [1, 2]. Several variants of light-sheet microscopy have been developed for more convenient sample access during imaging [3, 4, 5, 6, 7, 8]. However, oblique plane microscopy (OPM) is a unique setup which performs light-sheet microscopy with a single objective facing a given sample, thus providing maximum steric access to the sample [9]. To achieve this, it combines the concepts of aberration free remote focusing and selective plane illumination microscopy (SPIM) [10, 11, 12]. In its original configuration, OPM performs 3D imaging by axial scan of the light-sheet, achieved by piezo mounted remote microscope objective [13, 14]. Remote objective's axial movement results in an absolutely tilt invariant axial scan of the generated oblique light-sheet, making 3D reconstruction simple and free of geometrical distortions. Recently, multiple alternate scan configurations have been implemented in OPM for a more convenient, lateral scan of the generated light-sheet (see Fig. 1). Swept confocally-aligned planar excitation (SCAPE) microscopy was the first among these to introduce a polygon scan mirror based reflective arrangement, leading to lateral scan of the light-sheet [15]. A second configuration demonstrated oblique scanning two-photon light-sheet fluorescence microscopy (OS-2P-LSFM), which made use of a refractive transmission window for lateral scan of the light-sheet [16]. However, these scan arrangements were associated with several limitations. SCAPE introduced a scan position dependent tilt variation in the light-sheet, which is suboptimal for geometrical distortion free 3D imaging. The refractive window solution provided an absolutely tilt invariant scan for the excitation light-sheet, but not for the imaging path. Since this type of imaging relies on a relatively wide range (wavelength) of fluorescence signals, optical dispersion and aberrations (primarily spherical) are generated because of high refractive index glass window in the imaging path.

To combine the best features of the previous two arrangements, we introduced a plane mirror based scanned oblique plane illumination (SOPi) microscopy [17, 18]. Our work focused on optical ray tracing simulations to obtain an optimized scan geometry to resolve the tilt variance problem for both scanned illumination and descanned signal rays. Here, a plane mirror scanner is placed with its rotation axis at the intersection of the back focal plane (BFP) and the principal axis of the scan lens. In parallel, Yang *et al.* independently introduced epi-illumination SPIM (eSPIM) with a

plane mirror scanner for lateral scanning light-sheet [19]. However, eSPiM focused on solving the low effective numerical aperture issue of the OPM systems, and it did not delve into the scanner geometry. Subsequently, there has been a steady rise in the popularity of plane mirror scan geometry for creating systems with direct application in developmental biology and neuroscience. Two notable implementations include diffractive OPM and SCAPE 2.0 [20, 21]. Diffractive OPM performs single objective light-sheet imaging with low numerical aperture objectives and results in a very large field of view imaging in small organisms. SCAPE 2.0 demonstrates the rapid imaging capability of lateral scan architecture in OPM by imaging unrestricted small organisms at cellular resolution.

Given the challenges of the first two scan geometries in Fig. 1, plane mirror scan geometry is poised to become the preferred arrangement in future developments in this family of imaging techniques. However, plane mirror scanner geometry has not yet been studied in sufficient detail, in order to understand the underlying principles and, most importantly, the limitations of this scan geometry in OPM. Here, we perform a detailed geometrical analysis of this scan arrangement. We derive a relationship for evaluating tilt variance in scanned light-sheet. We also perform an experiment to measure the actual variation in the tilt of an oblique beam and cross validate the derived relationship. We then use the derived relationship to arrive at an optimized scanner placement. In addition to addressing tilt invariance in oblique light-sheet scanning, we also evaluate optical aberrations and field of view in the optimized system during a lateral scan.

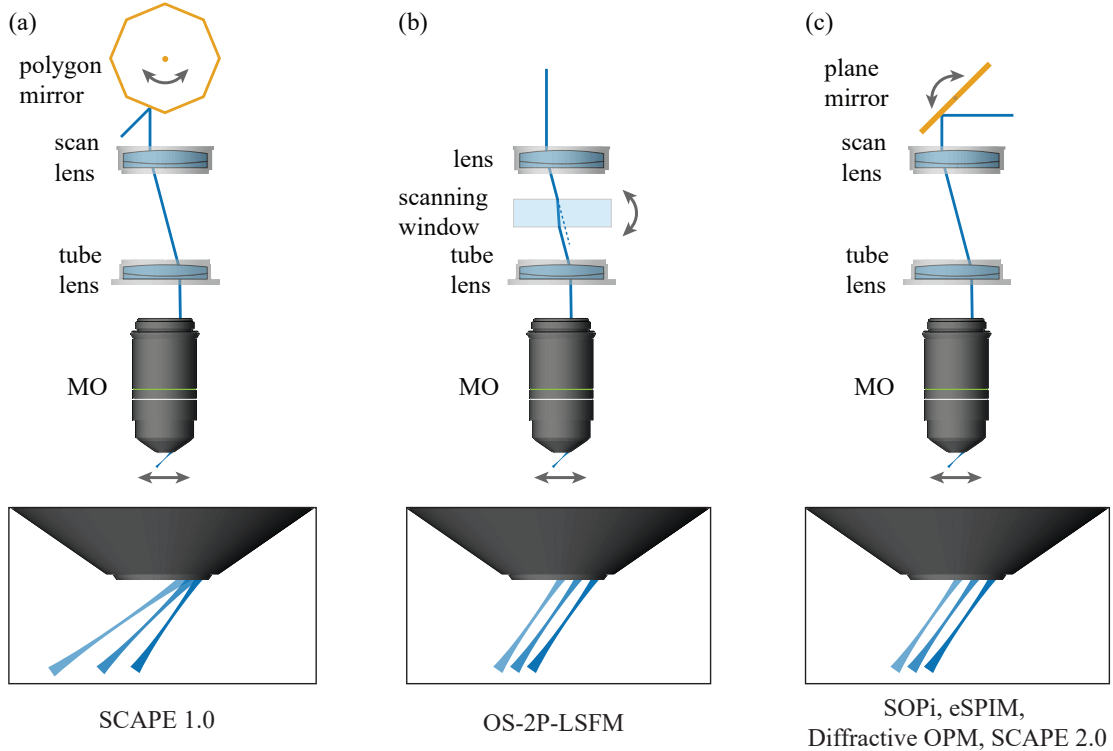


Fig. 1: Existing geometries for lateral scan of the generated light-sheet in OPM inspired systems. Insets show corresponding light-sheet scan orientations. (a) First arrangement uses a polygon mirror scanner to perform a lateral scan with varying tilt [15]. (b) Second arrangement uses a refractive transmission scanning window to perform constant tilt lateral scan [16]. (c) Third arrangement uses a plane mirror scanner to aim for constant tilt lateral scan [17, 18, 19, 20, 21]. MO: microscope objective.

2 Geometrical investigations of tilt invariant lateral scan and imaging

Geometrical optics is a simple yet powerful tool for analyzing optical systems. These intuitive analyses describe light as optical rays which travel in straight lines, bending or reflecting at interfaces, governed by well-known laws of refraction and reflection. Geometrical analysis is capable of investigating

imaging performance and aberrations in an optical system [22]. Various ray tracing software, which are industry and research standards for optical system design and optimization, rely on concepts from geometrical optics [23]. In our earlier work, we performed ray tracing based optimization for arriving at the SOPi arrangement [17]. It remains unknown whether the scan is absolutely tilt invariant, and if not, its deviation from expected ideal behavior. Therefore, in this section we build a thorough geometrical analysis of the plane mirror based scanner, aimed towards tilt invariant scan through an optical lens. We analyze the behavior of optical rays in a single plane first, as their extension into a light-sheet configuration is straightforward.

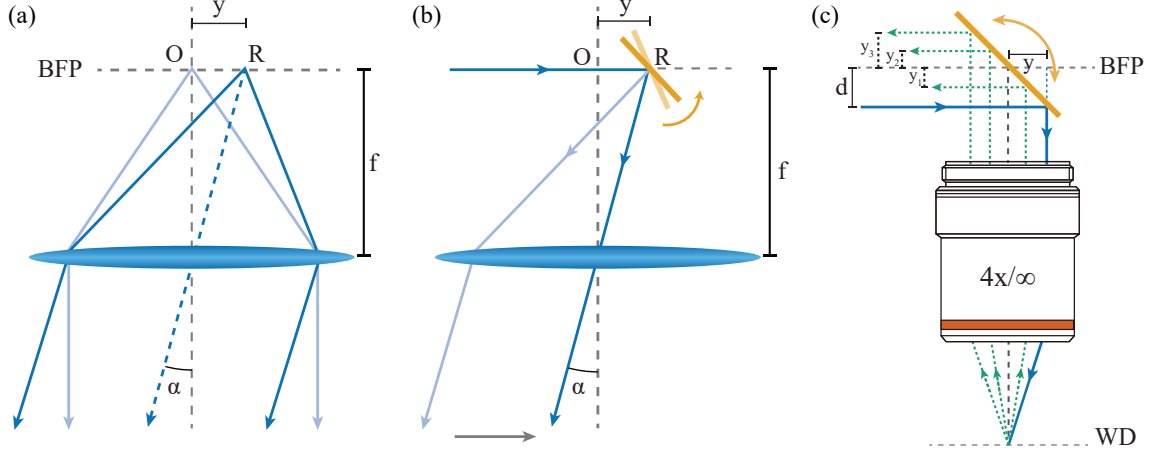


Fig. 2: Lens as an optical Fourier transforming element for tilt invariant scan and imaging. (a) A point source at the BFP leads to collimated optical rays where the lateral offset location of point source determines tilt angle of collimated rays. (b) A mirror scanner centered at the BFP leads to an absolutely tilt invariant lateral scan. (c) SOPi scan geometry under consideration for tilt invariant scan and imaging. WD: working distance.

2.1 Ideal lens, Fourier transform, and tilt invariant lateral scan

An optical lens is well known to behave as a Fourier transforming element [24]. A point source placed on the BFP of an ideal thin lens (optical aberration free) provides a set of collimated optical rays. As shown in Fig. 2(a), a point source offset by distance y leads to collimated optical rays with tilt angle α . In other words, if an optical ray emerges from a lens with a known tilt α , it can be uniquely associated with an offset point R on the BFP which is $y = f \times \tan(\alpha)$ distance apart from the principal axis, where f is the focal length of the lens. This property of an optical lens can be built upon to describe an ideal tilt invariant scan. Let us consider a planar mirror scanner placed with its rotation axis at R (on the BFP) as shown in Fig. 2(b). A laser beam hits the scanner at R , to get reflected towards the lens. Since the pivot point of reflected ray is fixed at R (on the BFP), it leads to a constant tilt lateral scan beyond the lens. This tilt angle

$$\alpha = \tan^{-1} \left(\frac{y}{f} \right), \quad (1)$$

can be easily changed by shifting the scanner and hence the optical beam pivot point R along the BFP.

2.2 Tilt invariant lateral scan and imaging

The geometry shown in Fig. 2(b) provides an absolutely tilt invariant scan of the oblique illumination beam. However, OPM is not limited to the consideration of excitation beam alone. It also requires consideration of the signal rays, arising due to optical scattering or emitted fluorescence from the sample. Unlike excitation beam, signal rays in OPM are not confined to a particular tilt angle. Therefore, we need an optical scanner which provides tilt invariant scanning/descanning for a wide range of beam offsets. Figure 2(c) shows the SOPi arrangement under consideration for this task. An

infinity corrected microscope objective serves as a Fourier transforming scan lens, and a plane mirror with its rotation axis at the intersection of the BFP and the principal axis operates as a scanner. A beam (blue line) with offset y forms an oblique illumination beam, and signal optical rays (green dotted) emerge at various tilt angles, where each tilt angle corresponds to a unique offset value y_1, y_2, y_3 , etc. What remains to be determined is how the beam offset and therefore tilt angle of the optical rays change during scanning. Tilt variance in oblique optical beam would lead to distorted 3D scan of the sample, while beam offset dependent tilt variance would cause additional optical aberrations [23].

2.3 Geometrical derivation

In this section we derive the relationship for scan dynamics of an optical beam in the SOPi geometry (Fig. 2(c)). For a generalized approach, we consider a scan geometry where the rotation axis of the scanner O is offset by d_y and d_z lengths along y and z axis, respectively. Figure 3 shows the magnified geometrical optics picture of this arrangement. OL and KL represent the horizontal and vertical offsets of scanner rotation axis from the intersection point of the principal axis and the BFP, respectively. Thus, $OL = d_y$ and $KL = d_z$. An optical ray MN is incident parallel to the BFP with an offset d from the scanner rotation axis O . This ray crosses the principal axis at M and hits the 45° tilted scan mirror (light orange) at P to get reflected vertically downwards along the z axis. When extended, the reflected beam meets the BFP at R . Thus, $ON \perp NP$, $NP \perp PR$, $KM = PR = d + d_z$, and $ON = LM = NP = d$. We now consider a new scanner position (dark orange) with the tilt angle $45^\circ + \theta$. Following the laws of reflection, the optical ray now hits the scanner at Q and is reflected, making an angle 2θ with the z axis. This reflected optical ray, when traced backwards, meets the BFP at S . T is the intersection point of both reflected rays where $\angle PTQ = \angle RTS = 2\theta$. For an ideal scanner geometry, R and S should overlap, leading to a constant offset and hence an absolutely tilt invariant scan. However, in practice, the gap RS dictates the error, or tilt variance, during the scan.

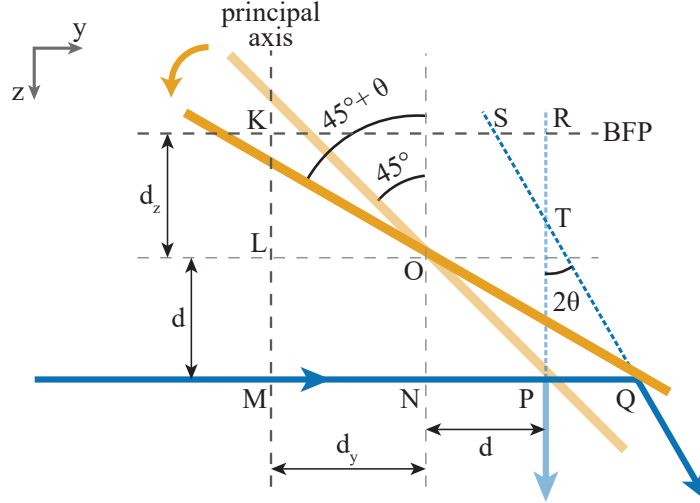


Fig. 3: A generalized SOPi scan geometry for the evaluation of tilt variance.

In $\triangle ONQ$ we have $\tan(\angle NOQ) = NQ/ON = (NP + PQ)/ON = 1 + PQ/d$. Therefore, $PQ = d \times (\tan(\angle NOQ) - 1) = d \times (\tan(45^\circ + \theta) - 1) = d \times [(1 + \tan\theta)/(1 - \tan\theta) - 1]$.

Or,

$$PQ = \frac{2d \times \tan\theta}{1 - \tan\theta}. \quad (2)$$

In $\triangle TPQ$ we have $\tan(\angle PTQ) = PQ/PT = PQ/(PR - RT) = PQ/(d + d_z - RT)$. Therefore, $RT = d + d_z - PQ/\tan(\angle PTQ) = d + d_z - PQ/\tan(2\theta)$. Replacing PQ from Eq. 2 and expanding $\tan(2\theta)$ we get $RT = d + d_z - d \times (1 + \tan\theta)$. Or,

$$RT = d_z - d \times \tan\theta. \quad (3)$$

In $\triangle TRS$ we have $RS = RT \times \tan(\angle RTS)$. Or,

$$RS = (d_z - d \times \tan\theta) \times \tan(2\theta), \quad (4)$$

where we replaced RT from Eq. 3. Here, we can use RS to precisely calculate tilt variance in the oblique optical beam during scan. The practical value of scan angle is $\theta < 5^\circ$, implying that RS is smaller than d_z . If f is the focal length of the Fourier transforming lens, we can use Eq. 1 to express tilt variance in an optical beam as a difference between beam tilt for two values of the mirror tilt *i.e.*, $\delta = [\alpha_0 - \alpha_\theta] = [\tan^{-1}(KR/f) - \tan^{-1}(KS/f)]$, where α_0 and α_θ correspond to 45° and $(45^\circ + \theta)$ mirror tilt angles, respectively. Rewriting KR and KS we have

$$\delta = \left[\tan^{-1} \left(\frac{d + d_y}{f} \right) - \tan^{-1} \left(\frac{d + d_y - RS}{f} \right) \right]. \quad (5)$$

In a practical case, Fourier transforming lenses have much longer focal lengths, compared to beam offsets and scanner position offsets (*e.g.* ref. [18] used $f = 100$ mm and offset $d = 3.54$ mm). Therefore, we have $(d + d_y)/f \ll 1$ and $(d + d_y - RS)/f \ll 1$ leading to the following small angle approximation $\delta \approx (d + d_y)/f - (d + d_y - RS)/f = RS/f$. Or, replacing RS from Eq. 4 we have

$$\delta \approx \left[\frac{d_z \times \tan(2\theta)}{f} - \frac{d \times \tan(\theta) \times \tan(2\theta)}{f} \right], \quad (6)$$

where δ is in radians.

Several considerations follow from Eq. 6. For a given practical value of tilt angle ($\theta < 5^\circ$), the first term of the equation is at least one order of magnitude larger than the second term. This implies that d_z plays a greater role in tilt variance. On the other hand, the second term is responsible for beam offset dependent tilt variance, and it may lead to optical aberrations in the system. Notably, tilt variance of the system increases with scan angle θ . On a closer inspection of Eq. 6 (and Eq. 4), it becomes clear that $d_z = (d \times \tan\theta)$ makes RS zero, leading to an absolutely tilt invariant scan. However, this relationship cannot be satisfied for a wide range of θ unless $d_z = d = 0$. This happens when both the incident beam and the rotation axis of the scanner are aligned to the BFP, *i.e.* the ideal scan condition as shown in Fig. 2(b). If θ is restricted to small values, a nonzero d is allowed when d_z approaches zero. This optimized case matches the schematic shown in Fig. 2(c), and is consistent with the previously published geometry of SOPi [17, 18]. We can further conclude from the expression for RS that an offset along lateral direction (d_y) does not change tilt variance in the system. However, a non-zero d_y would change overall tilt of the oblique beam (see Eq. 1) and an off-axis placement of the scanner would make the imaging system asymmetric. Therefore, the optimal scanning arrangement is one with $d_y = d_z = 0$. Here, the tilt variance expression from Eq. 5 becomes

$$\delta = \left[\tan^{-1} \left(\frac{d}{f} \right) - \tan^{-1} \left(\frac{d - RS}{f} \right) \right], \quad (7)$$

which under large focal length and small offsets approximation reduces to $\delta \approx RS/f = -d/f \times \tan(\theta) \times \tan(2\theta)$. Note that δ is in radians here. Considering an extreme example with a large scan angle $\theta = 10^\circ$, a large offset $d = 10$ mm, and $f = 100$ mm, we get tilt variance $\delta \approx 0.37^\circ$. This value of tilt variance is small for most practical purposes. However, based on subsequent optical elements, tilt variance can get magnified to become substantial. For example, the SOPi setup in ref. [17] introduces $22.22\times$ angular magnification, leading to effective $\sim 8.2^\circ$ tilt variance in the sample volume for the theoretical case described above.

3 Experimental validation

Next, we performed an experimental validation of the derived tilt variance relationship. For this we needed a Fourier transforming lens, a plane mirror based scanner, and a method for measuring the beam tilt angle α . The schematics of the setup are shown in Fig. 3. We used a low magnification, long working distance microscope objective ($4\times$, 0.1 NA, $f = 50$ mm, $WD = 30$ mm, Nikon) as a Fourier transforming lens. The advantage of using a low magnification objective is that its BFP lies outside the body of the objective and is therefore directly accessible without the need for a pair of lenses to relay it to the scanner. A galvanometer mounted plane mirror (QS12, 10 mm aperture, Nutfield) served as the scanner. Since the precise placement of the galvo scanner was crucial, we first

directed a collimated laser beam backwards through the microscope objective. This beam converged at the BFP of the objective, where the galvo scanner was carefully aligned to match the convergence point at the BFP with its rotation axis. We used a HeNe laser (HNL100L, Thorlabs) for alignment and experiment. We used a neutral density filter (not shown in figure) to reduce the laser power and reflected the laser beam towards the galvo scanner using a mirror mounted on a manual translation stage. This precision translation stage helped in varying the offset d for the incident laser beam. We used a precision translation stage mounted camera as a tool for measuring the outgoing beam tilt α . As shown in Fig. 4(a), the camera sensor plane was oriented perpendicular to the principal axis, and it served to capture beam position at two predefined positions $\pm p$ distance away from the working distance of the microscope objective. This arrangement enabled the calculation of beam tilt

$$\alpha = \tan^{-1} \left(\frac{\Delta}{2p} \right), \quad (8)$$

where Δ is the absolute shift between the beam positions on the two planes (see inset Fig. 3).

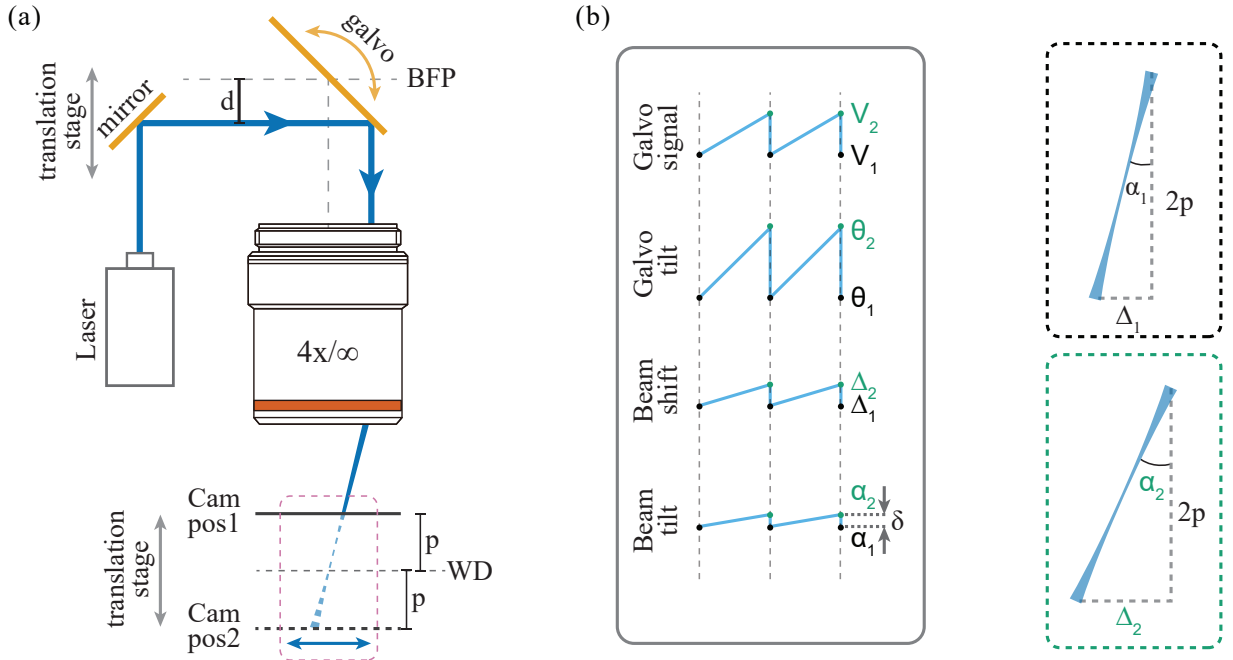


Fig. 4: Experimental strategy for evaluation of tilt variance. (a) Schematic of the experimental setup for measuring tilt variance. (b) Dependencies between voltage applied to galvo, galvo tilt, and beam shift/tilt.

We used a camera with $3.45 \mu\text{m}$ pixel size (Blackfly, BFS-U3-16S2M-CS, FLIR) and $p = 10 \text{ mm}$ for our experiments. This arrangement has beam tilt measurement resolution of $\sim 0.01^\circ$. Since beam divergence led to large beam size on camera, the center of each circular spot was noted as the beam position. As depicted in Fig. 4(b), the beam tilt measurements at two extreme scan points corresponding to galvanometer tilts θ_1 (for V_1 voltage) and θ_2 (for V_2 voltage) determined the tilt variance

$$\delta_{exp} = \alpha_2 - \alpha_1 = \tan^{-1} \left(\frac{\Delta_2}{2p} \right) - \tan^{-1} \left(\frac{\Delta_1}{2p} \right), \quad (9)$$

where $\Delta \ll 2p$ invokes small angle approximation leading to $\delta_{exp} = (\Delta_2 - \Delta_1)/2p$ (in radians). During experiments, a third precision translation stage (not shown in figure) helped shift the microscope objective and hence control d_z . Even with careful alignment of the camera linear translation stage, a slight angular mismatch in its translation axis and the microscope objective's principal axis is unavoidable. This mismatch gives rise to a consistent offset in the beam position, when measured at two camera positions. This offset is a constant value that can be easily compensated for by recording the on-axis beam positions (with $d = 0 \text{ mm}$) at the two planes.

We performed experiments for $d_z = 0 \text{ mm}$ and $d_z = 8 \text{ mm}$. For each of these cases, we recorded the beam positions on two planes ($2p = 20 \text{ mm}$ apart), with two voltages $V_{1,2} = \pm 0.4$, and four

Table 1: Calculation of Tilt Variance During Scan

d_z (mm)	d (mm)	δ_{th}	Δ_1 (px)	Δ_2 (px)	δ_{exp}
0	0	0.00°	0	-5	-0.05°
0	1	0.00°	170	164	-0.06°
0	2	0.00°	244	237	-0.07°
0	3	0.00°	367	360	-0.07°
8	0	0.59°	-28	25	0.53°
8	1	0.59°	88	142	0.54°
8	2	0.59°	201	255	0.54°
8	3	0.59°	315	370	0.55°

offset values $d = 0$ mm, 1 mm, 2 mm, and 3 mm. For each of these combinations, we obtained Δ_1 and Δ_2 as displayed in the unit of pixels (px) in Table 1. We experimentally measured the galvanometer’s tilt angle θ as $\pm 0.92^\circ$, in response to the applied ± 0.4 V. This was determined by measuring the deflection in galvanometer reflected laser beam, propagating through air onto a distal screen, in response to the applied voltage and using $\theta = 0.5 \times \tan^{-1}(\text{deflection} \div \text{screen distance}) = 0.5 \times \tan^{-1}(\pm 2.4 \text{ mm} / 74.5 \text{ mm})$. We confirmed that the small angle approximation is valid with our choice of parameters. For example, the experimental case with $d_z = 8$ mm, $d = 3$ mm, $f = 50$ mm and $\theta = \pm 0.92^\circ$ yields very similar values for δ_{th} as 0.587° (using Eq. 5), and 0.589° (using Eq. 6). We used Eq. 6 to calculate δ_{th} values in Table 1. We filled in Δ_1 and Δ_2 values from the experimental measurements of beam positions and used Eq. 9 to calculate δ_{exp} .

It is evident from Table 1 that the theoretical and experimental values of tilt variances tightly match. Moreover, it is clear that tilt variance is mainly dependent on d_z and has negligible dependence on beam offset d . A closer inspection shows that δ_{exp} is consistently offset along one direction from δ_{th} (average offset = -0.06°). This consistent offset can be explained by an unintentional residual d_z remaining in the setup during galvanometer alignment. In fact, Eq. 6 translates -0.06° offset in δ into $-800 \mu\text{m}$ offset in d_z . Therefore, galvanometer position can be compensated by this length to obtain a perfect alignment for tilt invariant scan. This analysis highlights the following aspects of SOPi microscopy. First, the SOPi system is highly sensitive to galvanometer positioning. Second, even careful experimental alignment may not be precise enough to obtain tilt invariant scan. Third, measurement of tilt variance during scan, combined with our derived relationships, can be used for precise measurement and correction of galvanometer position. Fourth, tilt variance for the corrected system can approach zero, leading to a practically tilt invariant scan.

4 Optical aberrations and field of view during SOPi scan

We have demonstrated that the SOPi scan geometry can offer tilt invariant scanning and imaging with an oblique light-sheet. However, it remains important to consider any limitations of this scan geometry. In this section we assess the effects of scanning on optical aberrations and field of view. We continue with a geometrical optics approach for these analyses.

4.1 Optical aberrations during scanning

Optical aberrations in a lens can be evaluated by tracing a pencil of parallel optical rays and observing how well they converge [25, 23]. An unaberrated optical lens leads all of the parallel rays to converge to a single point. Any deviation from this behavior is credited to the presence of optical aberrations. To evaluate optical aberrations due to the previously described scan arrangement, we consider an optical aberrations free lens in the optimized scan geometry where $d_z = 0$. This leads to $RS = -d \times \tan\theta \times \tan(2\theta)$ (from Eq. 4), and corresponding tilt variance $\delta = RS/f = -d/f \times \tan\theta \times \tan(2\theta)$ (from Eq. 6). There remains a residual tilt variance term which is proportional to d . In other words, an optical ray undergoes different amount of tilt variance based on its offset position from the principal axis. At first, it appears that this beam offset dependent tilt variance would lead to optical aberrations

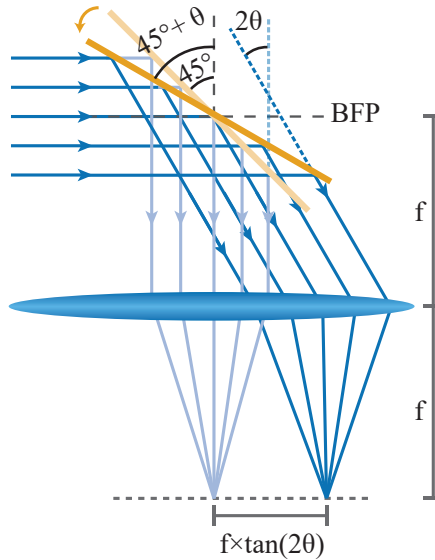


Fig. 5: Effect of lateral scanning on optical aberrations.

in the system. However, this is not the case. A pencil of optical rays get stretched (or compressed) based on the offset of individual rays. This stretching causes a change in tilt of the rays beyond the lens. Figure 5 shows that all optical rays, following the law of reflection, make a constant 2θ angle with the principal axis. This angle is independent of offset d . Therefore, these rays perfectly converge to a point on the focal plane, $f \times \tan(2\theta)$ away from the principal axis. It is important to note that we have considered an ideal optical lens. A real optical lens may show some deviation from these ideal characteristics due to the presence of optical aberrations within the lens. However, the plane mirror scanner arrangement does not add any optical aberrations.

4.2 Three dimensional field of view during scan

So far we have seen that SOPi arrangement provides tilt invariant lateral scan and adds no optical aberrations in the system. Next, we consider the field of view (FOV) characteristics of SOPi arrangement. A microscope objective is designed for a particular FOV which, as illustrated in Fig. 6(a), is specified as a disk of certain diameter at the working distance of the objective. A point lying outside the FOV is not imaged sharply, due to clipping of a subset of optical rays, *i.e.* vignetting. SOPi and related systems perform 3D imaging, requiring a consideration of the 3D FOV. Moreover, even the 2D FOV of the system is unusual due to the oblique nature of the light-sheet, requiring careful consideration.

Figure 6(b) shows the set of all acceptance cones through the 2D FOV of the microscope objective. For illustration purposes, we have shown a cross section view with the edges of each cone and have made them equidistant within the region. Clearly, any point lying outside the crossed lines region will not get completely covered by the total acceptance cone angle of the objective. Therefore, 3D FOV of the system is essentially a double cone shaped region as shown on the right in Fig. 6(b). In Fig. 6(c) we see that the double cone shape is made of two identical cones of height $FOV \div (2 \times \tan\beta)$ joined at their bases. Here, $\beta = \sin^{-1}(NA/n)$ is the half acceptance angle of the imaging system. All points inside this double cone 3D FOV are imaged sharply by a SOPi-like microscope. At a given scan position, 2D FOV would be represented by the intersection of 3D FOV and the light-sheet plane. Thus, 2D FOV in SOPi microscopy varies with lateral scan position and tilt angle of the light-sheet, potentially limiting the overall system lateral scan range. Figure 6(d) shows the effective 2D FOV of a SOPi-like microscopy at various lateral scan positions. It is apparent that the lateral scan range is large for thin samples and reduces with an increase in sample thickness (z -axis range).

Note that within this 3D FOV, the effective NA of the system depends on selection of the optical elements. SOPi's effective NA can be calculated using *Crossbill Design*, a Python based, platform independent, user friendly GUI for designing oblique light-sheet microscopes [26].

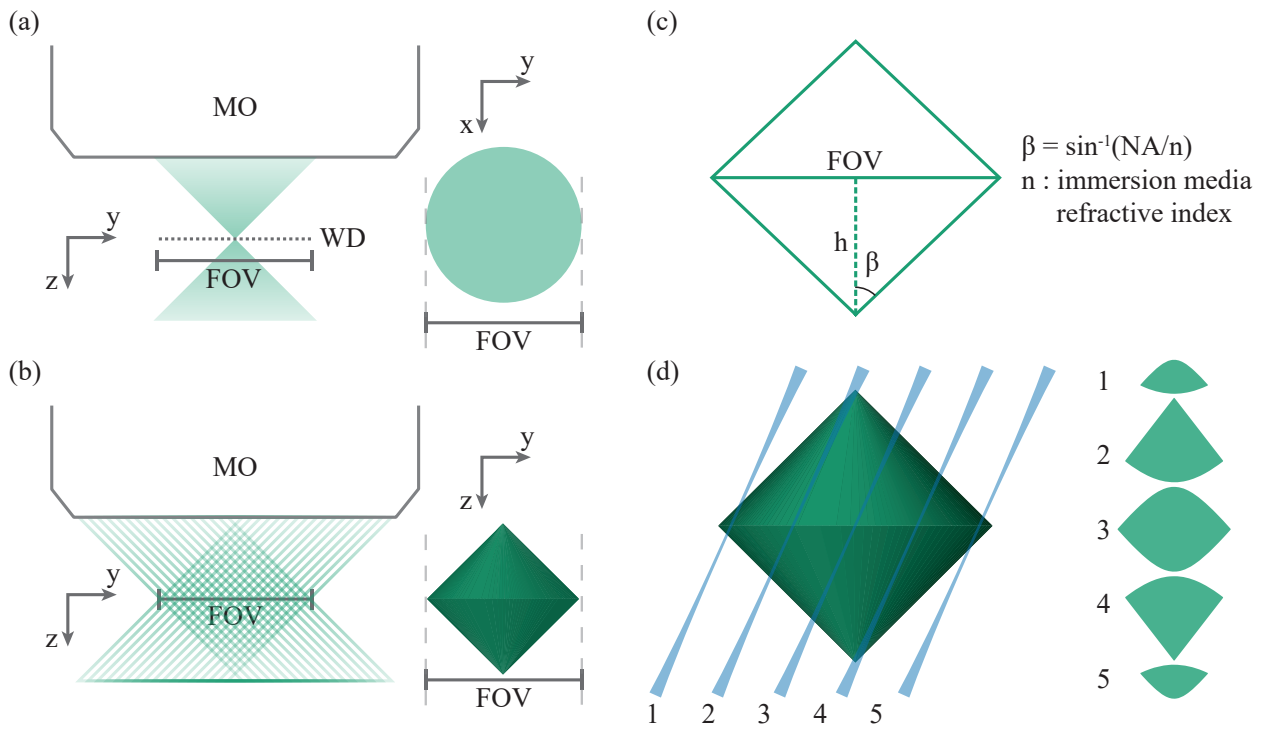


Fig. 6: 3D field of SOPi-like microscopy. (a) Acceptance cone of a microscope objective and corresponding two dimensional field of view. (b) A complete picture of acceptance cones through two dimensional field of view, where the overlapping region (double-cone shape) defines the three dimensional field of view. (c) Relationship between 2D field of view, numerical aperture, and 3D field of view. (d) Light-sheet orientation and corresponding cross-sectional field of view during lateral scan in SOPi microscopy.

5 Conclusion

We have performed a detailed geometrical analysis of tilt variance in scanned oblique plane microscopy, defined the optimal layout analytically, developed an experimental method and performed a measurement of tilt variance in a specific objective and scanner arrangement. These results confirm that essentially tilt invariant scanning can be achieved by lateral scan implementations of OPM inspired systems, but highlight the importance of precise scanner positioning and alignment for tilt variance and imaging performance control. Moreover, the experimental measurement of tilt variance, combined with our derived analytical relationship, can be used as a tool for precision alignment and positioning of scanners in these systems. We have also pointed out the absence of additional optical aberrations, important 3D FOV features, and lateral scan range constraints for this class of scanning arrangements.

Funding

NIH R01MH117111; Arnold and Mabel Beckman Foundation (Beckman Young Investigator Award); Kinship Foundation (Searle Scholar Award); and Rita Allen Foundation (Rita Allen Scholar Award).

References

- [1] Henry Siedentopf and Richard Zsigmondy. Über sichtbarmachung und größenbestimmung ultramikroskopischer teilchen, mit besonderer anwendung auf goldrubingläser. *Annalen der Physik*, 315(1):1–39, 1902.
- [2] Arne H Voie, DH Burns, and FA Spelman. Orthogonal-plane fluorescence optical sectioning: Three-dimensional imaging of macroscopic biological specimens. *Journal of microscopy*, 170(3):229–236, 1993.

- [3] Yicong Wu, Alireza Ghitani, Ryan Christensen, Anthony Santella, Zhuo Du, Gary Rondeau, Zhirong Bao, Daniel Colón-Ramos, and Hari Shroff. Inverted selective plane illumination microscopy (ispim) enables coupled cell identity lineaging and neurodevelopmental imaging in *caenorhabditis elegans*. *Proceedings of the National Academy of Sciences*, 108(43):17708–17713, 2011.
- [4] Yicong Wu, Peter Wawrzusin, Justin Senseney, Robert S Fischer, Ryan Christensen, Anthony Santella, Andrew G York, Peter W Winter, Clare M Waterman, Zhirong Bao, et al. Spatially isotropic four-dimensional imaging with dual-view plane illumination microscopy. *Nature biotechnology*, 31(11):1032, 2013.
- [5] Terrence F Holekamp, Diwakar Turaga, and Timothy E Holy. Fast three-dimensional fluorescence imaging of activity in neural populations by objective-coupled planar illumination microscopy. *Neuron*, 57(5):661–672, 2008.
- [6] Makio Tokunaga, Naoko Imamoto, and Kumiko Sakata-Sogawa. Highly inclined thin illumination enables clear single-molecule imaging in cells. *Nature methods*, 5(2):159–161, 2008.
- [7] Bianca Migliori, Malika S Datta, Christophe Dupre, Mehmet C Apak, Shoh Asano, Ruixuan Gao, Edward S Boyden, Ola Hermanson, Rafael Yuste, and Raju Tomer. Light sheet theta microscopy for rapid high-resolution imaging of large biological samples. *BMC biology*, 16(1):57, 2018.
- [8] Adam K Glaser, Nicholas P Reder, Ye Chen, Chengbo Yin, Linpeng Wei, Soyoung Kang, Lindsey A Barner, Weisi Xie, Erin F McCarty, Chenyi Mao, Aaron R. Halpern, Caleb R. Stoltzfus, Jonathan S. Daniels, Michael Y. Gerner, Philip R. Nicovich, Joshua C. Vaughan, Lawrence D. True, and Jonathan T. C. Liu. Multi-immersion open-top light-sheet microscope for high-throughput imaging of cleared tissues. *Nature communications*, 10(1):1–8, 2019.
- [9] C Dunsby. Optically sectioned imaging by oblique plane microscopy. *Optics express*, 16(25):20306–20316, 2008.
- [10] Edward J Botcherby, Rimas Juskaitis, Martin J Booth, and Tony Wilson. Aberration-free optical refocusing in high numerical aperture microscopy. *Optics letters*, 32(14), 2007.
- [11] Edward J Botcherby, R Juškaitis, Martin J Booth, and Tony Wilson. An optical technique for remote focusing in microscopy. *Optics Communications*, 281(4):880–887, 2008.
- [12] Jan Huiskens, Jim Swoger, Filippo Del Bene, Joachim Wittbrodt, and Ernst HK Stelzer. Optical sectioning deep inside live embryos by selective plane illumination microscopy. *Science*, 305(5686):1007–1009, 2004.
- [13] Sunil Kumar, Dean Wilding, Markus B Sikkell, Alexander R Lyon, Ken T MacLeod, and Chris Dunsby. High-speed 2d and 3d fluorescence microscopy of cardiac myocytes. *Optics express*, 19(15):13839–13847, 2011.
- [14] Markus B Sikkell, Sunil Kumar, Vincent Maioli, Christina Rowlands, Fabiana Gordon, Sian E Harding, Alexander R Lyon, Kenneth T MacLeod, and Chris Dunsby. High speed s-cmos-based oblique plane microscopy applied to the study of calcium dynamics in cardiac myocytes. *Journal of biophotonics*, 9(3):311–323, 2016.
- [15] Matthew B Bouchard, Venkatakaushik Voleti, César S Mendes, Clay Lacefield, Wesley B Grueber, Richard S Mann, Randy M Bruno, and Elizabeth MC Hillman. Swept confocally-aligned planar excitation (scape) microscopy for high-speed volumetric imaging of behaving organisms. *Nature photonics*, 9(2):113, 2015.
- [16] Younghoon Shin, Dongmok Kim, and Hyuk-Sang Kwon. Oblique scanning 2-photon light-sheet fluorescence microscopy for rapid volumetric imaging. *Journal of biophotonics*, 11(5):e201700270, 2018.

- [17] Manish Kumar, Sandeep Kishore, Jordan Nasenbeny, David L McLean, and Yevgenia Kozorovitskiy. Integrated one-and two-photon scanned oblique plane illumination (sopi) microscopy for rapid volumetric imaging. *Optics express*, 26(10):13027–13041, 2018.
- [18] Manish Kumar and Yevgenia Kozorovitskiy. Tilt-invariant scanned oblique plane illumination microscopy for large-scale volumetric imaging. *Optics letters*, 44(7):1706–1709, 2019.
- [19] Bin Yang, Xingye Chen, Yina Wang, Siyu Feng, Veronica Pessino, Nico Stuurman, Nathan H Cho, Karen W Cheng, Samuel J Lord, Linfeng Xu, et al. Epi-illumination spim for volumetric imaging with high spatial-temporal resolution. *Nature methods*, 16(6):501, 2019.
- [20] Maximilian Hoffmann and Benjamin Judkewitz. Diffractive oblique plane microscopy. *Optica*, 6(9):1166–1170, 2019.
- [21] Venkatakaushik Voleti, Kripa B Patel, Wenze Li, Citlali Perez Campos, Srinidhi Bharadwaj, Hang Yu, Caitlin Ford, Malte J Casper, Richard Wenwei Yan, Wenxuan Liang, et al. Real-time volumetric microscopy of in vivo dynamics and large-scale samples with scape 2.0. *Nature methods*, 16(10):1054–1062, 2019.
- [22] Max Born and Emil Wolf. *Principles of optics: electromagnetic theory of propagation, interference and diffraction of light*. Elsevier, 2013.
- [23] Robert Edward Fischer, Biljana Tadic-Galeb, and Paul R Yoder. *Optical System Design*. SPIE Press, 2008.
- [24] Joseph W Goodman. *Introduction to Fourier optics*. Roberts and Company Publishers, 2005.
- [25] Virendra N Mahajan. *Aberration theory made simple*. SPIE Press, 1991.
- [26] Manish Kumar and Yevgenia Kozorovitskiy. Crossbill design. Zenodo (2019), <https://doi.org/10.5281/zenodo.3543786>.